6th European Conference on Computational Mechanics (ECCM 6)
7th European Conference on Computational Fluid Dynamics (ECFD 7)
1115 June 2018, Glasgow, UK

WALL-RESOLVED AND WALL-MODELED ILES BASED ON HIGH-ORDER DG

RALF HARTMANN[1]

[1]DLR (German Aerospace Center)
Institute of Aerodynamics and Flow Technology
Lilienthalplatz 7, 38104 Braunschweig, Germany
ralf.hartmann@dlr.de, www.dlr.de

Key words: Discontinuous Galerkin method, ILES, wall-modeled LES

Abstract. In wall-modeled large eddy simulations (WM-LES) based on wall-stress-models, flow scales are resolved in the outer boundary layer and modeled in the inner layer. In order to avoid the so-called "log-layer mismatch", we take the thickness h_{wm} of the wall-modeled layer not to be the typically used frist grid layer thickness, but we take it independent of the grid as 20% of the boundary layer thickness. Important input to the wall-shear-stress approach is the near-wall velocity profile for which various approximations exist. In this work, we compare the results of the wall-shear-stress approach with the near-wall velocity profile given by Reichardt's law to the results of the wall-shear-stress approach where the near-wall velocity profile is given by DNS data. The WM-LES approach is implemented in the context of implicit large eddy simulations (ILES) based on high-order Discontinuous Galerkin methods. Numerical results are shown for the periodic channel flow. Comparisons are given for wall-modeled ILES to ILES (without wall-model) as well as to DNS data.

1 INTRODUCTION

Nowadays, large eddy simulations (LES) are feasible for flows of low and moderate Reynolds numbers. For high Reynolds number flows they are computationally too expensive due to the grid resolution requirements near the walls. Wall-modeled large eddy simulations (WM-LES) offer a way to reduce the resolution requirements near the wall and thus the computational cost.

In this work we consider a WM-LES method based on wall-stress-models. The basic idea in WM-LES is to resolve the flow scales in the outer boundary layer ($y > h_{wm}$) and to model the inner layer ($y < h_{wm}$) where $h_{wm} = 0.2\delta$ is the thickness of the wall-modeled layer and δ is the boundary layer thickness. In a wall-stress-model approach the no-slip wall boundary condition is replaced by a slip-wall boundary condition and the viscous boundary flux is modified according to a shear stress at the wall. The wall stress to be prescribed at a boundary point is obtained from a given near-wall velocity profile with input data taken from the flow field at a point located in a distance of h_{wm} normal to

the wall. Particular emphasis in this work is laid on h_{wm} being defined without reference to the computational mesh. In particular, we do not take h_{wm} to be the first cell layer thickness, like in e.g. [2], but we take $h_{wm} = 0.2\delta$ due to which the input data to the near-wall velocity profile might originate from several (possibly in the order of 10) near-wall cell layers distance from the wall boundary. As argued in Larsson et al.[6], h_{wm} being defined grid independent allows to generate grid converged WM-LES results which requires a first layer thickness $h_1 < h_{wm}$ and avoids the so-called "log-layer mismatch". In addition, not requiring $h_{wm} = h_1$ increases the flexibility of grids usable in this WM-ILES approach which significantly simplifies the generation of new grids.

In this work the WM-LES approach is implemented in the context of implicit large eddy simulations (ILES) based on high-order Discontinuous Galerkin methods.

In the following, we introduce the notations and the compressible Navier-Stokes equations in Section 2. We give details on the wall-modeled ILES approach in Sections 3, details on the spatial and temporal discretization in Section 4, and we show numerical results in Section 5 applying the approach to the channel flow test case at a friction Reynolds number of $Re_\tau = 395$.

2 THE COMPRESSIBLE NAVIER-STOKES EQUATIONS

We consider the compressible Navier-Stokes equations

$$\frac{\partial \mathbf{u}}{\partial t} + \nabla \cdot (\mathcal{F}^c(\mathbf{u}) - \mathcal{F}^v(\mathbf{u}, \nabla \mathbf{u})) = 0 \quad \text{in } \Omega. \tag{1}$$

Here, the vector of conservative variables $\mathbf{u}$, the convective flux $\mathcal{F}^c = (\mathbf{f}_1^c, \mathbf{f}_2^c, \mathbf{f}_3^c)$, and the diffusive flux $\mathcal{F}^v = (\mathbf{f}_1^v, \mathbf{f}_2^c, \mathbf{f}_3^c)^\top$ are given by

$$\mathbf{u} = \begin{bmatrix} \rho \\ \rho v_i \\ \rho E \end{bmatrix}, \quad \mathbf{f}_j^c(\mathbf{u}) = \begin{bmatrix} \rho v_j \\ \rho v_i v_j + p\delta_{ij} \\ \rho H v_j \end{bmatrix}, \quad \mathbf{f}_j^v(\mathbf{u}, \nabla \mathbf{u}) = \begin{bmatrix} 0 \\ \tau_{ij} \\ \tau_{jk} v_k + \mathcal{K} T_{x_j} \end{bmatrix}, \tag{2}$$

for $i, j = 1, 2, 3$, where ρ, $\mathbf{v} = (v_1, v_2, v_3)^\top$, p and E denote the density, velocity vector, pressure and specific total energy, respectively. Here, H is the specific total enthalpy given by $H = E + \frac{p}{\rho} = e + \frac{1}{2}\mathbf{v}^2 + \frac{p}{\rho}$ where e is the specific static internal energy. The pressure is determined by the equation of state of an ideal gas $p = (\gamma - 1)\rho e$, where $\gamma = c_p/c_v$ is the ratio of specific heat capacities at constant pressure, c_p, and constant volume, c_v; for dry air, $\gamma = 1.4$. Furthermore, the viscous stress tensor is given by $\underline{\tau} = \mu \underline{S}$ where μ is the dynamic viscosity coefficient, and $\underline{S} = \nabla \mathbf{v} + (\nabla \mathbf{v})^\top - \frac{2}{3}(\nabla \cdot \mathbf{v}) I$ the traceless strain tensor. Finally, $\mathcal{K}$ is the thermal conductivity coefficient, and the temperature T is given by $e = c_v T$ where $\mathcal{K} T = \frac{\mu\gamma}{Pr}\left(E - \frac{1}{2}\mathbf{v}^2\right)$, and $Pr = \frac{\mu c_p}{\mathcal{K}} = 0.72$ is the Prandtl number.

The compressible Navier-Stokes equations (1) on the domain $\Omega \subset \mathbb{R}^3$ are subject to boundary conditions on the boundary $\Gamma = \partial\Omega$, in particular, periodic boundary conditions on $\Gamma_{\text{periodic}} \subset \Gamma$, and no-slip (vanishing velocity) wall boundary conditions and adiabatic conditions,

$$\mathbf{v} = 0, \quad \mathbf{n} \cdot \nabla T = 0, \tag{3}$$

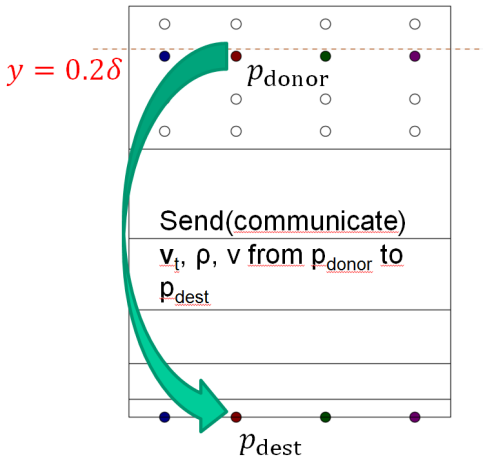

Figure 1: Flow field data at p_{donor} is used to define the viscous flux in the boundary point p_{dest}.

at adiabatic walls $\Gamma_{\text{W,adia}} \subset \Gamma$. Here, the viscous flux in normal direction reduces to

$$\mathbf{n} \cdot \mathcal{F}^v(\mathbf{u}, \nabla\mathbf{u}) = (0, (\underline{\tau}\mathbf{n})_i, \mathbf{n} \cdot (\underline{\tau}\mathbf{v}))^\top, \tag{4}$$

with $(\underline{\tau}\mathbf{n})_i = \tau_{ij} n_j$ and $\mathbf{n} \cdot (\underline{\tau}\mathbf{v}) = n_j \tau_{jk} v_k$.

3 THE WALL-STRESS-MODEL APPROACH

In the wall-stress-model approach considered the no-slip wall boundary condition is replaced by a slip (vanishing normal velocity, $\mathbf{n} \cdot \mathbf{v} = 0$) wall boundary condition, and instead of prescribing the two tangential velocity components to zero the boundary flux is modified to prescribe a specific wall shear stress τ_w at the boundary.

While the shear stress evaluated directly at the wall is subject to an underresolved turbulent flow close to the wall, the basic idea in the wall-stress-model approach is that information for the evaluation of an improved value of τ_w is taken from the flow field in a region close to the wall but sufficiently far from the wall such that flow scales are resolved. Typically this information is retrieved from the flow field in a distance of 0.2δ from the wall, where δ is the boundary layer thickness.

In detail, the wall-stress-model approach considered consists of following steps: For each integration point p_{dest} on a wall-modeled boundary face:

1. (In a pre-processing step) find a point p_{donor} normal to the wall in a distance of (approx.) $y = 0.2\delta$ to p_{dest}.

2. From the solution (instantaneous flow field) at point p_{donor} (cf. Figure 1) take

   - the tangential velocity $\mathbf{v}_t = (I - \mathbf{n} \times \mathbf{n})\mathbf{v}$,
   - the density ρ, the kinematic viscosity ν, and
   - the distance $y = \text{dist}(p_{\text{donor}}, p_{\text{dest}})$.

3. Solve $u^+(y^+) = |\mathbf{v}_t|/u_\tau$ with $y^+ = yu_\tau/\nu$ for the friction velocity u_τ by solving

$$F(u_\tau) = |\mathbf{v}_t|/u_\tau - u^+(yu_\tau/\nu) = 0 \tag{5}$$

   for u_τ using Newton's method.

4. Compute the wall shear stress $\tau_w = \rho u_\tau^2$.

5. In p_{dest} apply a slip-wall boundary condition and a viscous numerical flux $\mathbf{n} \cdot \mathcal{F}^v$ with prescribed τ_w.

Here, $u^+(y^+)$ with $u^+ = u/u_\tau$ and $y^+ = yu_\tau/\nu$ is the near-wall velocity profile for which various algebraic approximations are available, e.g.

- the logarithmic law-of-wall (log-law): $u^+(y^+) = \min(y^+, \ln(y^+)/\kappa + c)$, and
- the Reichardt's law-of-wall: $u^+(y^+) = \ln(1+\kappa y^+)/\kappa + A(1-e^{-y^+/B} - y^+/Be^{-y^+/C})$.

Note, that in Section 5 we compare our numerical solutions against these algebraic approximations with the Karman constant $\kappa = 0.38$ and the constant $c = 4.1$ [8], and $A = c - \ln(\kappa)/\kappa$, $B = 11$ and $C = 3$ [2].

At the wall-modeled boundary the viscous (normal and adiabatic) flux (4) is replaced by a viscous flux which prescribes the wall shear stress τ_w (cf. Step 5 above). For this, we split the vector $\underline{\tau}\mathbf{n}$ into a wall normal and a wall tangential part as follows

$$\underline{\tau}\mathbf{n} = (\underline{\tau}\mathbf{n})_{\mathbf{n}} + (\underline{\tau}\mathbf{n})_t, \tag{6}$$

with $(\underline{\tau}\mathbf{n})_{\mathbf{n}} = (\mathbf{n} \otimes \mathbf{n})(\underline{\tau}\mathbf{n})$, and $(\underline{\tau}\mathbf{n})_t = (\mathbb{I} - \mathbf{n} \otimes \mathbf{n})(\underline{\tau}\mathbf{n})$, such that $(\underline{\tau}\mathbf{n})_t \cdot \mathbf{n} = 0$. Note, that the space of tangential vectors is a two-dimensional space. Given a (normalized) tangential velocity vector $\hat{\mathbf{v}}_t = \mathbf{v}_t/|\mathbf{v}_t|$, with $\mathbf{v}_t = (\mathbb{I} - \mathbf{n} \otimes \mathbf{n})\mathbf{v}$ one could further split $(\underline{\tau}\mathbf{n})_t$ into a part orthogonal and a part parallel to $\hat{\mathbf{v}}_t$,

$$\underline{\tau}\mathbf{n} = (\underline{\tau}\mathbf{n})_{\mathbf{n}} + (\underline{\tau}\mathbf{n})_{t,\hat{\mathbf{v}}_t^\perp} + (\underline{\tau}\mathbf{n})_{t,\hat{\mathbf{v}}_t^\parallel}. \tag{7}$$

For wall-modelled (I)LES the no-slip adiabatic boundary $\Gamma_{\text{W,adia}}$ with condition (3) is replaced by a slip-wall boundary $\Gamma_{\text{W,slip}}$ with condition $\mathbf{v} \cdot \mathbf{n} = 0$, and a viscous boundary flux is used including a prescribed tangential

$$(\underline{\tau}\mathbf{n})_t^{\text{wm}} = -\tau_w \hat{\mathbf{v}}_t, \tag{8}$$

where the wall shear stress τ_w value is obtained from a wall model. There are various possible formulations of the resulting viscous boundary flux (cf. Table 1). Given that the adiabatic no-slip wall boundary condition (3) prescribes four boundary quantities we prefer variant A) in Table 1 over the others due to the matching number of prescribed boundary quantities.

Table 1: Slip wall boundary with wall shear stress prescribing viscous boundary flux.

Variant	$\mathbf{v}\cdot\mathbf{n}=0$ and the viscous (normal) boundary flux given by	# of prescribed quantities	
A)	$\mathbf{n}\cdot\mathcal{F}^v = (0,\ (\underline{\tau}\mathbf{n})_n + (\underline{\tau}\mathbf{n})_t^{\mathrm{wm}},\ \mathbf{n}\cdot(\underline{\tau}\mathbf{v}))^\top$	4	✓
B)	$\mathbf{n}\cdot\mathcal{F}^v = (0,\ (\underline{\tau}\mathbf{n})_n + (\underline{\tau}\mathbf{n})_t^{\mathrm{wm}},\ \mathbf{n}\cdot(\underline{\tau}\mathbf{v}) + \mathcal{K}\mathbf{n}\cdot\nabla T)^\top$	3	✗
C)	$\mathbf{n}\cdot\mathcal{F}^v = (0,\ 0 + (\underline{\tau}\mathbf{n})_t^{\mathrm{wm}},\ \mathbf{n}\cdot(\underline{\tau}\mathbf{v}))^\top$	5	✗
D)	$\mathbf{n}\cdot\mathcal{F}^v = (0,\ (\underline{\tau}\mathbf{n})_n + (\underline{\tau}\mathbf{n})_{t,\hat{\mathbf{v}}_t^\perp} + (\underline{\tau}\mathbf{n})_t^{\mathrm{wm}},\ \mathbf{n}\cdot(\underline{\tau}\mathbf{v}))^\top$	3	✗

4 THE SPATIAL AND TEMPORAL DISCRETIZATION

The compressible Navier-Stokes equations (1) are discretized in space using the Discontinuous Galerkin (DG) method. To this end, let the domain Ω be subdivided into a shape-regular mesh $\mathcal{T}_h = \{\kappa\}$ consisting of (possibly curved) elements κ. Furthermore, let $\mathbf{V}_h^p$ be the finite element space consisting of discontinuous vector-valued polynomial functions of degree $p \geq 0$ on $\mathcal{T}_h$, then the DG discretization of (1) is given by (cf. [4, 5]): Find $\mathbf{u}_h$ in $\mathbf{V}_h^p$ such that

$$\int_\Omega \left(-\mathcal{F}^c(\mathbf{u}_h) + \mathcal{F}^v(\mathbf{u}_h, \nabla_h \mathbf{u}_h)\right) : \nabla_h \mathbf{v}_h \,\mathrm{d}\mathbf{x} + \sum_{\kappa\in\mathcal{T}_h} \int_{\partial\kappa} \left(\hat{\mathbf{h}}_h - \underline{\hat{\sigma}}_h \mathbf{n}\right)\cdot \mathbf{v}_h \,\mathrm{d}s + \sum_{\kappa\in\mathcal{T}_h} \int_{\partial\kappa} (\hat{\mathbf{u}}_h - \mathbf{u}_h)\otimes\mathbf{n} : \left(G^\top(\mathbf{u}_h)\nabla\mathbf{v}_h\right) \,\mathrm{d}s = 0 \quad (9)$$

for all $\mathbf{v}_h \in \mathbf{V}_h^p$, where $\mathbf{n}|_{\partial\kappa}$ denotes the outward unit normal vector to the boundary $\partial\kappa$ of element κ. Here, the convective and diffusive *numerical* flux functions, $\hat{\mathbf{h}}_h$ and $\underline{\hat{\sigma}}_h$, are approximations to the normal convective flux and the diffusive flux, $\mathbf{n}\cdot\mathcal{F}^c(\mathbf{u}_h)$ and $\mathcal{F}^v(\mathbf{u}_h, \nabla_h\mathbf{u}_h)$, respectively. On an interior face $\partial\kappa \cap \partial\kappa'$ between two neighboring elements $\kappa, \kappa' \in \mathcal{T}_h$, the numerical flux functions

$$\begin{aligned} \hat{\mathbf{h}}_h &= \hat{\mathbf{h}}(\mathbf{u}_h, \mathbf{n}) = \hat{\mathbf{h}}(\mathbf{u}_h^+, \mathbf{u}_h^-, \mathbf{n}), \\ \underline{\hat{\sigma}}_h &= \underline{\hat{\sigma}}(\mathbf{u}_h, \nabla\mathbf{u}_h) = \underline{\hat{\sigma}}(\mathbf{u}_h^+, \mathbf{u}_h^-, \nabla\mathbf{u}_h^+, \nabla\mathbf{u}_h^-), \end{aligned} \quad (10)$$

connect the interior and the exterior traces, $\mathbf{u}_h^+$ and $\mathbf{u}_h^-$, and their derivatives, $\nabla\mathbf{u}_h^+$ and $\nabla\mathbf{u}_h^-$, of $\mathbf{u}_h$. On a boundary face $\partial\kappa \cap \Gamma \neq \emptyset$, the numerical boundary flux functions,

$$\begin{aligned} \hat{\mathbf{h}}_h|_\Gamma &= \hat{\mathbf{h}}_{\Gamma,h} = \hat{\mathbf{h}}_\Gamma(\mathbf{u}_h^+, \mathbf{n}), \\ \underline{\hat{\sigma}}_h|_\Gamma &= \underline{\hat{\sigma}}_{\Gamma,h} = \underline{\hat{\sigma}}_\Gamma(\mathbf{u}_h^+, \nabla\mathbf{u}_h^+). \end{aligned} \quad (11)$$

depend on the interior trace $\mathbf{u}_h^+$, directly and/or through the boundary function $\mathbf{u}_\Gamma(\cdot)$ which on the wall boundary is given by

$$\mathbf{u}_\Gamma(\mathbf{u}_h) = (u_{h,1}, \mathbf{0}, u_{h,5})^\top \qquad \text{on } \Gamma_{\text{W,adia}}, \tag{12}$$

$$\mathbf{u}_\Gamma(\mathbf{u}_h) = \begin{pmatrix} 1 & \mathbf{0} & 0 \\ \mathbf{0} & \mathbb{I} - \mathbf{n}\otimes\mathbf{n} & \mathbf{0} \\ 0 & \mathbf{0} & 1 \end{pmatrix} \mathbf{u}_h \qquad \text{on } \Gamma_{\text{W,slip}}. \tag{13}$$

Similarly, the vector-valued numerical flux function $\hat{\mathbf{u}}_h$ in (9) is an approximation to $\mathbf{u}_h$ and is given by $\hat{\mathbf{u}}_h = \hat{\mathbf{u}}(\mathbf{u}_h) = \hat{\mathbf{u}}(\mathbf{u}_h^+, \mathbf{u}_h^-)$ on interior faces and by $\hat{\mathbf{u}}_h|_\Gamma = \hat{\mathbf{u}}_{\Gamma,h} = \hat{\mathbf{u}}_\Gamma(\mathbf{u}_h^+)$ on boundary faces. Finally, $G(\mathbf{u})$ denotes the homogeneity tensors defined by $\mathbf{f}_k^v(\mathbf{u}, \nabla\mathbf{u}) = G_{kl}(\mathbf{u})\partial\mathbf{u}/\partial x_l$, $k,l = 1,2,3$. Assuming that the numerical fluxes $\hat{\mathbf{h}}_h$ and $\hat{\underline{\sigma}}_h$ are consistent, then (9) is a consistent discretization (cf. [4]) of the flow equations (1). The total drag and lift coefficients, C_D and C_L, are given by

$$J(\mathbf{u}) = \int_{\Gamma_\text{W}} (p\,\mathbf{n} - \underline{\tau}\,\mathbf{n})\cdot\boldsymbol{\psi}\,\mathrm{d}s = \int_{\Gamma_\text{W}} (p\,n_i - \tau_{ij}n_j)\,\psi_i\,\mathrm{d}s, \tag{14}$$

where $\boldsymbol{\psi}$ is given by $\boldsymbol{\psi}_d = \frac{1}{C_\infty}(\cos(\alpha), 0, \sin(\alpha))^\top$ or $\boldsymbol{\psi}_l = \frac{1}{C_\infty}(-\sin(\alpha), 0, \cos(\alpha))^\top$ for the drag and lift coefficient, respectively, α is the angle of attack, and $C_\infty = q_\infty A$, where $q = \frac{1}{2}\rho|\mathbf{v}|^2$ denotes the dynamic pressure, A denotes a reference area and subscripts $_\infty$ indicate freestream quantities. Let the total force coefficients (14) be discretized by

$$J_h(\mathbf{u}_h) = \int_{\Gamma_\text{W}} \left(\hat{\mathbf{h}}_{\Gamma,h} - \hat{\underline{\sigma}}_{\Gamma,h}\mathbf{n}\right)\cdot\tilde{\boldsymbol{\psi}}\,\mathrm{d}s, \tag{15}$$

with $\tilde{\boldsymbol{\psi}} = (0, \boldsymbol{\psi}, 0)^\top$, then (9) is an adjoint consistent discretization (cf. [4]) of the flow equations (1) which is required for an optimal order of convergence of the force coefficients.

The discontinuous Galerkin discretization employed is based on an ortho-normalized basis defined in physical space. This non-parameteric approach is particularly well suited for agglomeration multigrid [1]. The Roe flux is used for convective terms, and the BR2 scheme with $C_{\text{br2}} = 2$ is employed for viscous terms. On (wall and periodic) boundaries the same numerical fluxes are taken like on interior faces [4]. According to (15) also the force coefficients are evaluated based on the same numerical boundary fluxes.

For the discretization in time we employ a 5-stage SDIRK (single coefficient diagonal implicit Runge-Kutta) method of order 4 (cf. Table 2 or [3]). The nonlinear problem in each stage of the implicit time iteration scheme is solved fully implicitely using a Backward-Euler iteration which recovers Newton's method for high CFL numbers. The linear problems in each of the implicit solver steps are solved with a block-Jacobi preconditioned GMRes method. The blocks are given by lines and are inverted using the Thomas' algorithm.

5 NUMERICAL RESULTS

5.1 The channel flow test case

The channel flow is considered in a box $[0, L_x]\times[0, L_y]\times[0, L_z]$ with $L_x = 6.4$, $L_y = 2\delta$, $L_z = 3.2$ and the boundary layer thickness $\delta = 1$ (cf. Figure 2). Top and bottom

Table 2: L-stable 5-stage SDIRK method of order 4 [3].

$\frac{1}{4}$	$\frac{1}{4}$				
$\frac{3}{4}$	$\frac{1}{2}$	$\frac{1}{4}$			
$\frac{11}{20}$	$\frac{17}{50}$	$-\frac{1}{25}$	$\frac{1}{4}$		
$\frac{1}{2}$	$\frac{371}{1360}$	$-\frac{137}{2720}$	$\frac{15}{544}$	$\frac{1}{4}$	
1	$\frac{25}{24}$	$-\frac{49}{48}$	$\frac{125}{16}$	$-\frac{85}{12}$	$\frac{1}{4}$
	$\frac{25}{24}$	$-\frac{49}{48}$	$\frac{125}{16}$	$-\frac{85}{12}$	$\frac{1}{4}$

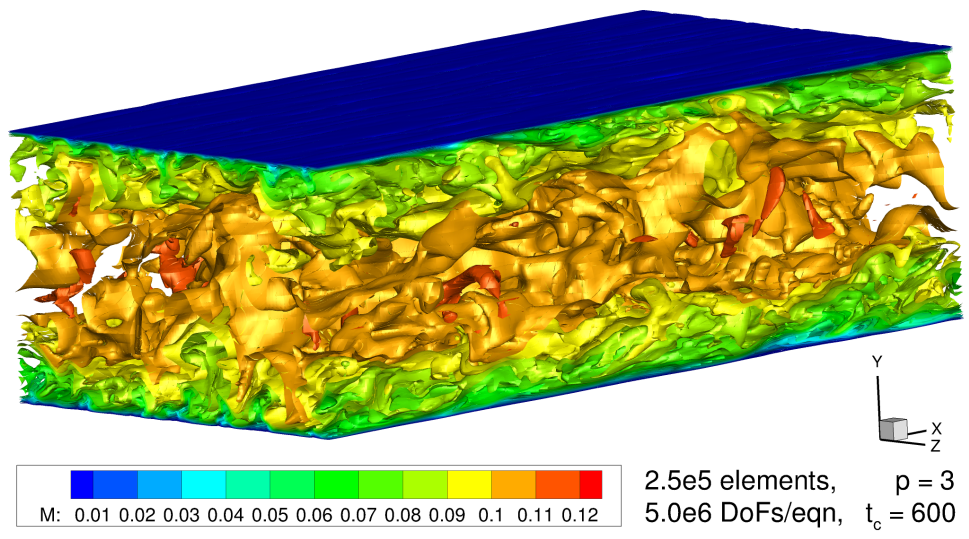

Figure 2: Channel flow at $Re_\delta = 6875$: Instantaneous flow field after 600 CTU.

boundaries are walls, all remaining boundaries are treated as periodic boundaries. In the following computational results the bulk Reynolds number $Re_\delta = U_{\text{bulk}}\delta/\nu$ and the Mach number M is prescribed. The flow is forced in x-direction by a non-vanishing pressure gradient dp/dx. Instead of the bulk velocity

$$U_{\text{bulk}} = 1/A_{\text{inflow}} \int_0^{L_z} \int_0^{L_y} u \, \mathrm{d}y \, \mathrm{d}z, \tag{16}$$

with $A_{\text{inflow}} = L_y L_z$ we consider the mass flow rate averaged over the domain

$$\dot{m} = 1/L_x \int_0^{L_z} \int_0^{L_y} \int_0^{L_x} \rho u \, \mathrm{d}x \, \mathrm{d}y \, \mathrm{d}z, \tag{17}$$

and impose the pressure gradient dp/dx such that the prescribed mass flow rate $\dot{m}$ is obtained. In each time step dp/dx is modified such that $\dot{m}$ is retained.

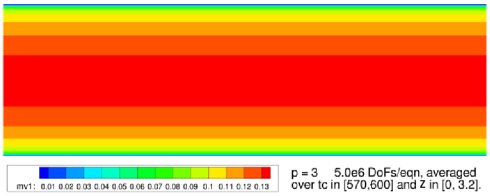

Figure 3: Channel flow at $Re_\delta = 6875$: Flow field averaged over $t_c \in [570, 600]$ and $z \in [0, L_z]$.

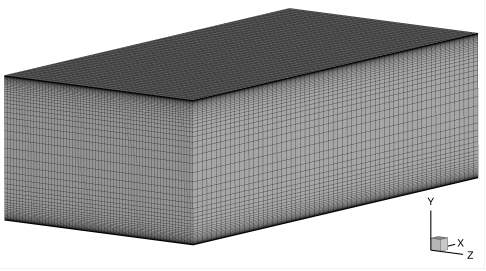

Figure 4: Grid for the channel flow: 61x64x64=249856 elements.

For post-processing the flow field is averaged over (a multiple of) 30 convective time units (CTU equals L_x/U), averaged over $z \in [0, L_z]$ (cf. Figure 3) and averaged over $x \in [0, L_x]$. From the averaged flow field we compute the viscous drag coefficient C_{df} and the wall shear stress τ_w from the viscous fluxes on the boundary. The friction velocity $u_\tau = \sqrt{\tau_w/\rho}$ then gives the resulting friction Reynolds number $Re_\tau = u_\tau \delta/\nu$.

In the following we consider the channel flow test case of at the friction Reynolds number (of approximately) $Re_\tau = 392$ and a Mach number $M = 0.1$. For this we prescribe the associated bulk Reynolds number $Re_\delta = 6875$ and measure the quality of the flow solution by considering the deviation of the friction Reynolds number obtained by our ILES and WM-ILES computations against the friction Reynolds number $Re_{\tau,\text{DNS}} = 392.24$ obtained in DNS computations by Moser [7].

5.2 Computational grid for the channel flow

For the channel flow test case at $Re_\tau = 392$ we consider a grid with $61 \times 64 \times 64 = 249856$ elements (cf. Figure 4). Originally being generated for hybrid RANS/LES computations [9], this grid has an $\Delta y^+ = 0.78$, $\Delta x^+ = 41.15$ and $\Delta z^+ = 19.61$ ($\Delta y = 0.002$, $\Delta x = 0.105$ and $\Delta z = 0.05$), and a Δy stretching factor of 1.14.

5.3 ILES reference computations

For the channel flow test case and the grid described in the previous two subsections we perform a series of ILES computations which will serve as reference solutions when jugding the quality of the WM-ILES computations in Section 5.4.

The 5-stage SDIRK method described in Section 4 is used with time step size $\Delta t_c = 0.01$

Table 3: Channel flow at $Re_\delta = 6875$: p-refinement on mesh of 61x64x64=249856 elements.

p	DoFs/eqn	p-ref. t_c	continued t_c	Re_τ
1	1.0e6	0 - 450		
			450 - 510	293.08
			510 - 570	291.23
2	2.5e6	450 - 480		
		480 - 540		379.88
			540 - 600	379.41
3	5.0e6	540 - 570		
			570 - 630	391.86
			630 - 690	392.48

(in convective time units). Each stage of this implicit RK method is solved using a (slightly regularized) Newton method (as given by a Backward-Euler iteration with CFL=10^{15}) up to a nonlinear residual of 10^{-4}. The (exact) Jacobian matrix is assembled once per timestep and 3 (line-preconditioned) GMRES iterations are performed on each linear system.

Using the DG discretization described in Section 4 we start from freestream with the ortho-normalized basis of polynomial degree 1 for 450 convective time units (CTU), subsequently performing two global p-refinements, we continue with a polynomial degree 2 for 90 CTU and with a polynomial degree 3 for another 30 CTU. The computations are then further continued for averaging the solutions and evaluating velocity correlations. Details of these computations are given in Table 3. For each of the polynomial degrees $p = 1, 2$ and 3 (column 1), it includes the number of degrees of freedoms per equation (DoFs/eqn) in colum 2, the simulation time in convective time units between p-refinement steps (col. 3) and for continued averaging (col. 4) and the friction Reynolds numbers obtained in column 5. Here, we see that while there is quite a large deviation of the resulting friction Reynolds numbers Re_τ for $p = 1$ and $p = 2$ from the friction Reynolds number $Re_{\tau,\mathrm{DNS}} = 392.24$ by Moser[7], they are quite close for $p = 3$. Mach number isosurfaces of the $p = 3$ (instantaneous) solution at $t_c = 600$ are shown in Figure 2.

The resulting averaged u-velocities are shown in Figure 5 together with the averaging period and the associated friction Reynolds numbers. Here, we see that while the $p = 1$ and $p = 2$ solution are quite far from the DNS solution, the $p = 3$ solution lies almost on top of the DNS solution. In Figure 5 each of the $p = 1, 2$ and 3 velocity profiles is normalized with the corresponding u_τ value which differs in the three computations and thus leads to different y^+ values of the opposite wall (between $y^+ = 600$ and $y^+ = 800$). The same data normalized with a common value $u_{\tau,\mathrm{DNS}}$ is shown in Figure 6. Finally, the Reynolds stresses $\overline{v_i' v_j'}^+$ for $p = 2$ and 3 are shown in Figure 7. Here, again, we see quite a difference between the $p = 2$ results and the DNS results, but recognize that the $p = 3$ results are very close to the DNS results.

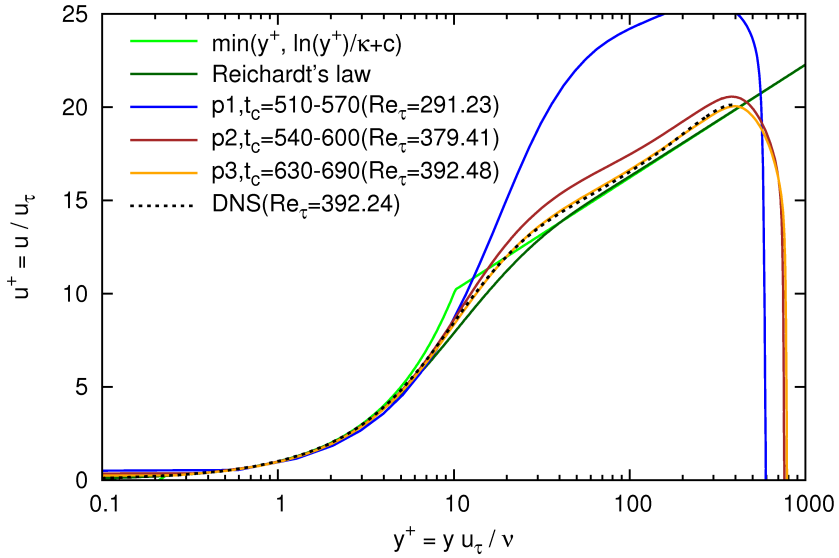

Figure 5: ILES for the channel flow: Velocity profiles $u^+(y^+)$ of averaged solutions of the $p = 1, 2$ and 3 computations compared to DNS[7]. Normalization of u^+ and y^+ is based on u_τ of the $p = 1, 2, 3$ computations.

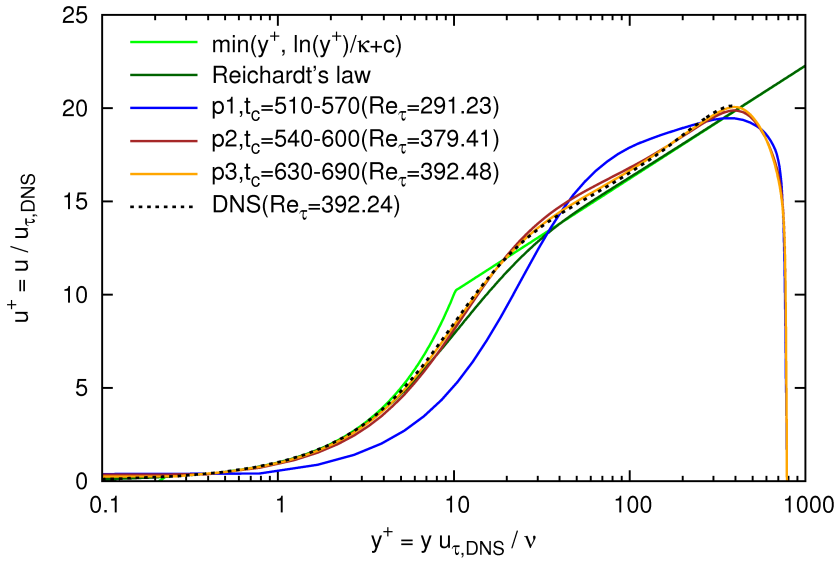

Figure 6: ILES for the channel flow: Velocity profiles $u^+(y^+)$ of averaged solutions of the $p = 1, 2$ and 3 computations compared to DNS[7]. Normalization of u^+ and y^+ is based on $u_{\tau,\mathrm{DNS}}$.

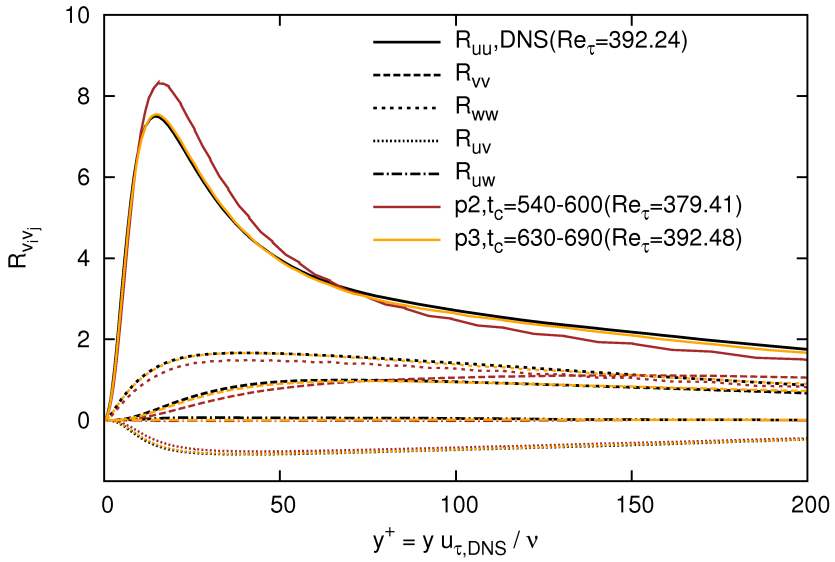

Figure 7: ILES for channel flow: Reynolds stresses $\overline{v_i' v_j'}^+$ of the $p = 2$ and 3 computations compared to DNS[7]. Normalization is based on $u_{\tau,\mathrm{DNS}}$.

5.4 WM-ILES computations

In this section we now employ the wall-shear-stress approach described in Section 3 on the channel flow. In particular, we consider the wall-stress-model approach with the near-wall velocity profile $u^+(y^+)$ given by Reichardt's law. As Reichardt's law represents an approximation only to the "exact" velocity profile as given by DNS (cf. Figure 5), we consider the wall-shear-stress approach also with Reichardt's law replaced by DNS data. This allows us to investigate the difference incurred by considering an approximation (like Reichardt's law) only to the near-wall velocity profile, and the maximal theoretical improvement which could be achieved when considering an improved(optimal) model of the near-wall velocity profile.

Like for the LES computations in Section 5.3 we start from freestream with the wall-shear-stress approach based on Reichardt's law with $p = 1$, and subsequently increase the polynomial degree to $p = 2$ and $p = 3$. Then each of the $p = 1, 2$ and 3 computations are further continued for averaging. We perform the same steps independently for the wall-shear-stress approach with $u^+(y^+)$ given by DNS data. The resulting friction Reynolds numbers are collected in Table 4. For each polynomial degree it includes the number of degrees of freedom per equation, the friction Reynolds numbers Re_τ obtained by ILES, and those obtained by the two versions of WM-LES together with the deviation of the Re_τ values from $Re_{\tau,\mathrm{DNS}}$ given as percentages. Here we see that the Re_τ values obtained by WM-LES are higher while those of ILES are lower than $Re_{\tau,\mathrm{DNS}}$. However, the Re_τ values of WM-LES are closer to $Re_{\tau,\mathrm{DNS}}$ than those of ILES. This is clearly visible for $p = 1$ but still significant for $p = 2$. Furthermore, we see that the results of WM-ILES based on Reichardt's law are, as expected, not as good as those of WM-ILES with $u^+(y^+)$ given by

Table 4: Channel flow at $Re_\delta = 6875$: Comparison of friction Reynolds numbers for ILES and two versions of WM-ILES (once $u^+(y^+)$ is given by Reichardt's law and once given by DNS data) compared to $Re_{\tau,\mathrm{DNS}}$ [7]. Re_τ values are computed from solutions averaged over 60 CTU (for ILES) and 120 CTU (for WM-ILES). Deviations of computed Re_τ values from $Re_{\tau,\mathrm{DNS}}$ are given as percentages.

p	DoFs/ eqn	ILES Re_τ	WM-ILES $u^+(y^+)$=Reichardt Re_τ	WM-ILES $u^+(y^+)$=DNS data Re_τ	DNS [Moser et al.] $Re_{\tau,\mathrm{DNS}}$
1	1.0e6	293.08 (-25.3%)	415.24 (5.9%)	408.98 (4.3%)	
		291.23 (-25.8%)	418.81 (6.8%)	409.89 (4.5%)	
			415.09 (5.8%)	408.47 (4.1%)	
2	2.5e6	379.88 (-3.2%)	403.75 (2.9%)	400.42 (2.1%)	392.24
		379.41 (-3.3%)	404.93 (3.2%)	399.78 (1.9%)	
3	5.0e6	391.86 (-0.1%)			
		392.48 (0.06%)			

DNS data. Figure 8 shows the mean velocity profiles of the WM-LES computation based on Reichardt's law compared to those of ILES and DNS. Here, we see that in a large range below and above $y = 0.2\delta$ the WM-LES profiles are closer to DNS than the ILES profiles. This is clearly visible for $p = 1$, but a significant improvement is visible also for the $p = 2$ results. In fact, in a region close to $y = 0.2\delta$ the $p = 2$ results of WM-LES are almost on top of the $p = 3$ ILES results.

6 CONCLUSIONS

In the context of high-order Discontinuous Galerkin methods, we developed a wall-modeled ILES method based on wall-stress-models. The thickness h_{wm} of the wall-modeled layer is taken as $h_{wm} = 0.2\delta$ independent of the grid. We compared channel flow computations based on ILES with those based on two versions of WM-ILES. Comparison of our numerical results to DNS data shows that the WM-ILES computations give a significantly more accurate friction Reynolds number than the ILES computations. Furthermore, the WM-ILES approach with the near-wall velocity profile given by Reichardt's law is, as expected, not as accurate as the WM-ILES near-wall velocity profile given by DNS data. The difference between the two WM-ILES computations shows the maximal potential improvement in WM-ILES which could be gained by improving the approximate near-wall velocity profile like Reichardt's law.

Finally, we note that the computations shown were performed at a rather low Reynolds number for which the flow is almost resolved. It remains to investigate the applicability of the proposed approach to underresolved flows at higher Reynolds numbers.

ACKNOWLEDGEMENTS

This work was funded through the TILDA (Towards Industrial LES/DNS in Aeronautics - Paving the Way for Future Accurate CFD) project grant agree-

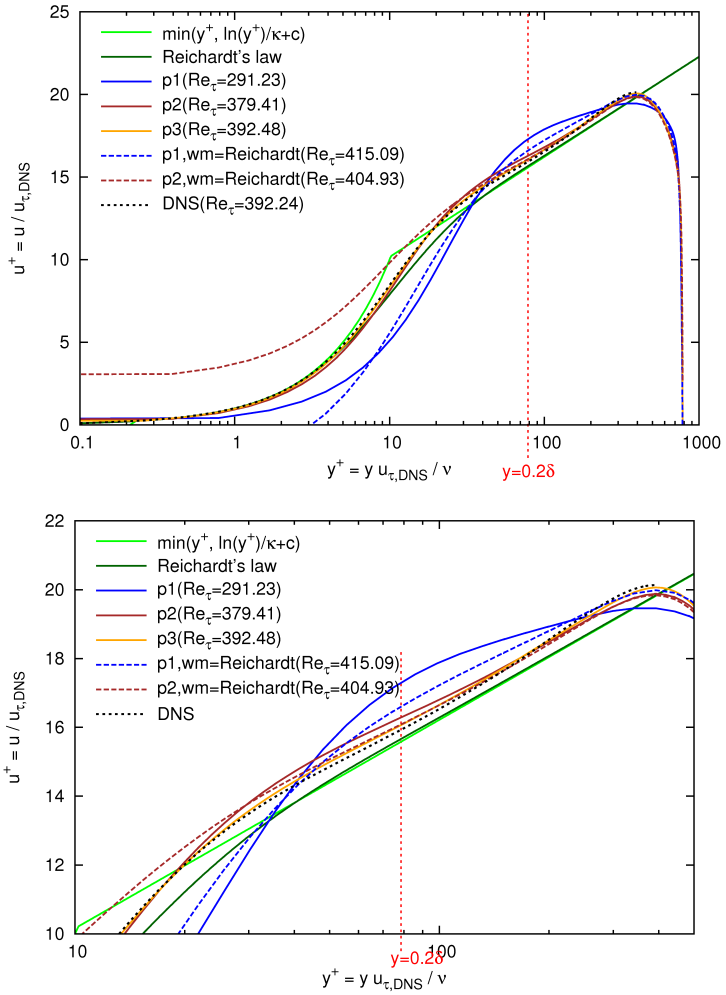

Figure 8: Channel flow: WM-ILES ($p = 1$ and $p = 2$ with wall model given by Reichardt's law) compared to ILES ($p = 1, 2$ and 3) and DNS[7].

ment number 635962, receiving funding from the European Unions Horizon 2020 research and innovation program.

REFERENCES

[1] F. Bassi, L. Botti, A. Colombo, D. D. Pietro, and P. Tesini. On the flexibility of agglomeration based physical space discontinuous Galerkin discretizations. *Journal of Computational Physics* (2012) **231**(1):45–65.

[2] A. Frère, C. C. de Wiart, K. Hillewaert, P. Chatelain, and G. Winckelmans. Application of wall-models to discontinuous Galerkin LES. *Physics of Fluids* (2017) **29**.

[3] E. Hairer and G. Wanner. *Solving Ordinary Differential Equations II. Stiff and Differential-Algebraic Problems*. Spinger, 2002.

[4] R. Hartmann and T. Leicht. Generalized adjoint consistent treatment of wall boundary conditions for compressible flows. *J. Comput. Phys.* (2015) **300**:754–778.

[5] R. Hartmann, H. McMorris, and T. Leicht. Curved grid generation and DG computation for the DLR-F11 high lift configuration. In M. Papadrakakis, V. Papadopoulos, G. Stefanou, and V. Plevris, editors, *Proceedings of the ECCOMAS Congress 2016, Crete Island, Greece, 5–10 June 2016* (2016).

[6] J. Larsson, S. Kawai, J. Bodart, and I. Bermejo-Moreno. Large eddy simulation with modeled wall-stress: recent progress and future directions. *Mech. Eng. Reviews* (2016) **3**(1).

[7] R. D. Moser, J. Kim, and N. N. Mansour. Direct numerical simulation of turbulent channel flow up to $Re_\tau = 590$. *Physics of Fluids* (1999) **11**(4):943–945.

[8] J. M. Österlund, A. V. Johansson, H. M. Nagib, and M. H. Hites. A note on the overlap region in turbulent boundary layers. *Phys. Fluids* (2000) **12**:1–4.

[9] A. Probst, J. Löwe, S. Reu, T. Knopp, and R. Kessler. Scale-resolving simulations with a low-dissipation low-dispersion second-order scheme for unstructured flow solvers. *AIAA Journal* (2016) **54**(10):2972–2987.